Check for updates

Crystal phase content-dependent functionality of dual phase SnO$_2$–WO$_3$ nanocomposite films *via* cosputtering crystal growth†

Yuan-Chang Liang (ID) * and Yu Chao

In this study, crystalline SnO$_2$–WO$_3$ nanocomposite thin films were grown through radio-frequency cosputtering of metallic Sn and ceramic WO$_3$ targets. The W content in the SnO$_2$ matrix was varied from 5.4 at% to 12.3 at% by changing the WO$_3$ sputtering power during thin-film growth. Structural analyses showed that increased WO$_3$ phase content in the nanocomposite films reduced the degree of crystallization of the SnO$_2$ matrix. Moreover, the size of the composite films' surface crystallites increased with WO$_3$ phase content, and the large surface crystallites were composed of numerous nanograins. Addition of WO$_3$ crystals to the SnO$_2$ matrix to form a composite film improved its light harvesting ability. The SnO$_2$–WO$_3$ nanocomposite films exhibited improved photodegradation ability for Rhodamine B dyes compared with their individual constituents (*i.e.*, SnO$_2$ and WO$_3$ thin films), which is attributable to the suitable type II band alignment between the SnO$_2$ and WO$_3$. Moreover, an optimal WO$_3$ phase content (W content: 5.4 at%) in the SnO$_2$ matrix substantially enhanced the ethanol gas-sensing response of the SnO$_2$ thin film. This suggested that the heterojunctions at the SnO$_2$/WO$_3$ interface regions in the nanocomposite film considerably affected its ethanol gas-sensing behavior.

Introduction

SnO$_2$ is an n-type semiconductor with a wide bandgap that can be used in numerous applications, such as gas sensor materials and photocatalysts.[1–3] A thin-film structure is a commonly used morphology for wide bandgap oxides in various technological applications. SnO$_2$ thin films have been prepared through various methods such as sputtering, chemical solution deposition, spray pyrolysis deposition, and the sol–gel process.[1,4–6] Of these methods, sputtering has the potential to synthesize oxide thin films with precise thickness control, tunable crystallinity, and large-area deposition. Sputtering SnO$_2$ thin films is therefore of potential interest for gas sensor and photocatalyst applications. However, improving the gas-sensing and photocatalytic properties of SnO$_2$ thin films to meet the requirements of such practical applications remains highly desirable. Doping impurity atoms into the SnO$_2$ matrix is a commonly used method for enhancing the gas-sensing and photodegradation properties of SnO$_2$ films. For example, Ce-doped SnO$_2$ thin films exhibit a superior ethanol gas-sensing response to that of pure SnO$_2$ thin films.[1] Ag-doped SnO$_2$ thin films have been synthesized through spray pyrolysis, demonstrating enhanced H$_2$S gas detection ability compared with that of pure SnO$_2$ thin films.[7]

Doping impurity atoms into SnO$_2$ lattices affects the crystal defects and surface morphology of SnO$_2$ thin films, thereby changing its gas-sensing ability. Furthermore, Fe- and Ni-co-doped SnO$_2$ sol–gel-derived thin films exhibit enhanced photocatalytic properties for organic dyes. The dopant modifies the optical bandgap of the SnO$_2$ thin film and enhances its light-harvesting and photocatalytic activity. However, research on a composite film structure containing a different phase in the SnO$_2$ matrix to improve gas-sensing and photodegradation properties for organic dyes has been limited. A SnO$_2$-based composite structure combining SnO$_2$ with another phase has been widely used in one-dimensional and sphere/particle morphologies to improve gas-sensing properties and dye photodegradation ability.[8,9] However, due to complex synthesis methods, such two-phase structures in thin films have seldom been reported. SnO–SnO$_2$ composite thin films have been shown to possess superior NO$_2$ sensing ability, and the formation of the SnO–SnO$_2$ junctions at the thin-film surface dominates their gas-sensing ability.[10] Sol–gel-derived SnO$_2$–TiO$_2$ composite thin films exhibit improved photodegradation ability for methyl orange, with an optimal phase content ratio.[11] Therefore, incorporating other oxide phases into the SnO$_2$ matrix to form SnO$_2$-based composite films for enhanced gas-sensing and photodegradation seems promising.

WO$_3$ is also an n-type semiconductor with a wide bandgap of approximately 2.6–3.6 eV that has been used in gas sensor and catalytic materials.[12,13] WO$_3$ thin films are usually prepared through sputtering methods.[14] The band alignment between

Institute of Materials Engineering, National Taiwan Ocean University, Keelung 20224, Taiwan. E-mail: yuanvictory@gmail.com

This journal is © The Royal Society of Chemistry 2019

Paper
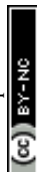
SnO_2 and WO_3 crystals exhibits a type II band heterojunction, and this composite system is reportedly beneficial in reducing the recombination rate of photogenerated carriers in films.[15] Additionally, hydrothermally derived WO_3–SnO_2 composite particles demonstrate superior sensing behavior toward various volatile organic compounds, compared with the constituent counterparts.[16] Similarly, hydrothermally derived WO_3–SnO_2 nanosheet composites exhibit better acetone gas-sensing behavior than their counterparts.[17] Developing a SnO_2–WO_3 two-phase composite film therefore has the potential to enhance gas-sensing responses and organic dye photo-degradation abilities. However, several literatures report the synthesis of SnO_2–WO_3 composite films through thermal evaporation and pulsed laser deposition with a fixed Sn/W composition source.[18,19] These are disadvantageous to modulate the relative phase contents in the composite thin film through a one-step process and are not good strategies to find optimal photodegradation and gas-sensing properties of the composite films associated with the phase content-dependent factors. Developing a single composite film with a SnO_2–WO_3 two-phase structure through a suitable method therefore has the potential to design and enhance gas-sensing responses and organic dye photodegradation abilities. In this study, SnO_2–WO_3 composite films with various WO_3 phase contents were prepared using dual-gun cosputtering. The advantage of the cosputtering method provides *in situ* modulation of the relative SnO_2/WO_3 phase contents during the synthesis of a single composite film. By adjusting sputtering power of the target, varying phase contents of the SnO_2 and WO_3 are designed and obtained in a single composite film. The effects of WO_3 phase content in the SnO_2 matrix on the microstructures and optical properties of composite films were investigated. The gas-sensing behavior and photodegradation rate of the nano-composite films were correlated with the WO_3 phase content-dependent microstructures and optical properties.

Experiments

SnO_2–WO_3 composite films with various WO_3 crystal contents were fabricated onto the glass and 300 nm-thick SiO_2/Si substrates using dual-gun sputtering system. Sn metallic disc and WO_3 ceramic disc with a size of 2 inches were used as sputtering targets to prepare SnO_2–WO_3 composite films. During growth of SnO_2–WO_3 composite films, the DC sputtering power of Sn target was fixed at 20 W; moreover, the radio-frequency (rf) sputtering power of WO_3 target varied from 35 to 65 W. The thin-films growth temperature was maintained at 500 °C with an Ar/O_2 ratio of 2 : 1; the gas pressure during thin-film deposition was fixed at 1.33 Pa. The distance between the target and substrate is fixed at 7 cm. The rotation speed of the sample holder is fixed at 5 rpm. The sputtering duration for the composite films was fixed at 20 min. The sputtering guns are set to an incline angle of 60° over the sample surface.

Sample crystal structures were investigated by X-ray diffraction (XRD; Bruker D2 PHASER) using Cu Kα radiation. The surface morphology of various thin films was investigated by scanning electron microscopy (SEM; Hitachi S-4800). The microstructures of the thin-film samples were characterized by high-resolution transmission electron microscopy (HRTEM; JEOL JEM-2100F). The TEM samples are prepared by dual-beam focused ion beam (FIB: FEI Nova NanoLab 200). The sputtering of top Au layer was performed using Cressington 108 sputter coater. The operating current is set as 40 mA and sputtering time is 15 s. The target and substrate distance is 3 cm; the working pressure is 6×10^{-2} mbar. The absorption spectra of thin-film samples were conducted by ultraviolet-visible spectroscopy (UV-Vis; Jasco V-750). X-ray photoelectron spectroscopy (XPS; PHI 5000 VersaProbe) analysis was used to determine the chemical compositions of various thin-film samples. The contact angle measurements were performed in atmospheric air at room temperature using a commercial contact angle meter with ±1° accuracy (CA; SEO Phoenix 300). To measure gas-sensing properties, the silver paste was coated onto the surface of the thin-film samples to form electrodes for gas-sensing measurements. The gas sensors made from various thin-film samples were placed in a closed vacuum chamber, and various concentrations of ethanol vapor (100, 250, 500, 750, and 1000 ppm) were introduced into the test chamber, using synthetic air as the carrier gas. The gas sensing response of the thin-film sensors to ethanol vapor is defined as the R_a/R_g. R_a is the sensor electrical resistance in the absence of target gas and R_g is that in the target gas. Photodegradation tests were performed by comparing the degradation of aqueous solution of Rhodamine B (RhB; 10^{-6} M) containing various thin-film samples under solar light irradiation excited from the 100 W Xe arc lamp. The solution volume of RhB is 20 ml and the sample size for photodegradation tests has a fixed coverage area of 1.5 cm × 1.5 cm.

Results and discussion

The XRD patterns of SnO_2 and composite SnO_2–WO_3 films prepared under various WO_3 sputtering powers are shown in Fig. 1(a)–(d). From Fig. 1(a), the Bragg reflections are ascribed to crystallographic planes of (110), (101), (200), (211) and (220) of tetragonal SnO_2 (JCPDS no. 00-002-1337). The sharp and distinct Bragg reflections originated from SnO_2 revealed that the as-deposited SnO_2 thin film is well crystalline and is in a polycrystalline structure. The SnO_2–WO_3 composite films grown under various WO_3 sputtering powers of 35–65 W exhibited a Bragg reflection centered at approximately 33° and is ascribed to monoclinic WO_3 (022) (JCPDS no. 01-089-4476). No other distinct Bragg reflection from impurity phase was observed, indicating that the composite films are composed of SnO_2 and WO_3 phases. Upon increasing the WO_3 sputtering power, the intensity of WO_3 (022) peak was gradually increased. Notably, the relative peak intensity of SnO_2 (110) is still more intense than that of WO_3 (022), showing that the SnO_2 is a dominant phase in the composite film. Well crystalline composite films were successfully prepared herein. The crystallite sizes of SnO_2 and WO_3 are further calculated by using Debye–Scherrer equation.[20] The SnO_2 film has an average crystallite size of approximately 20 nm. Notably, the average SnO_2 and WO_3 crystallite sizes decreased during the cosputtering
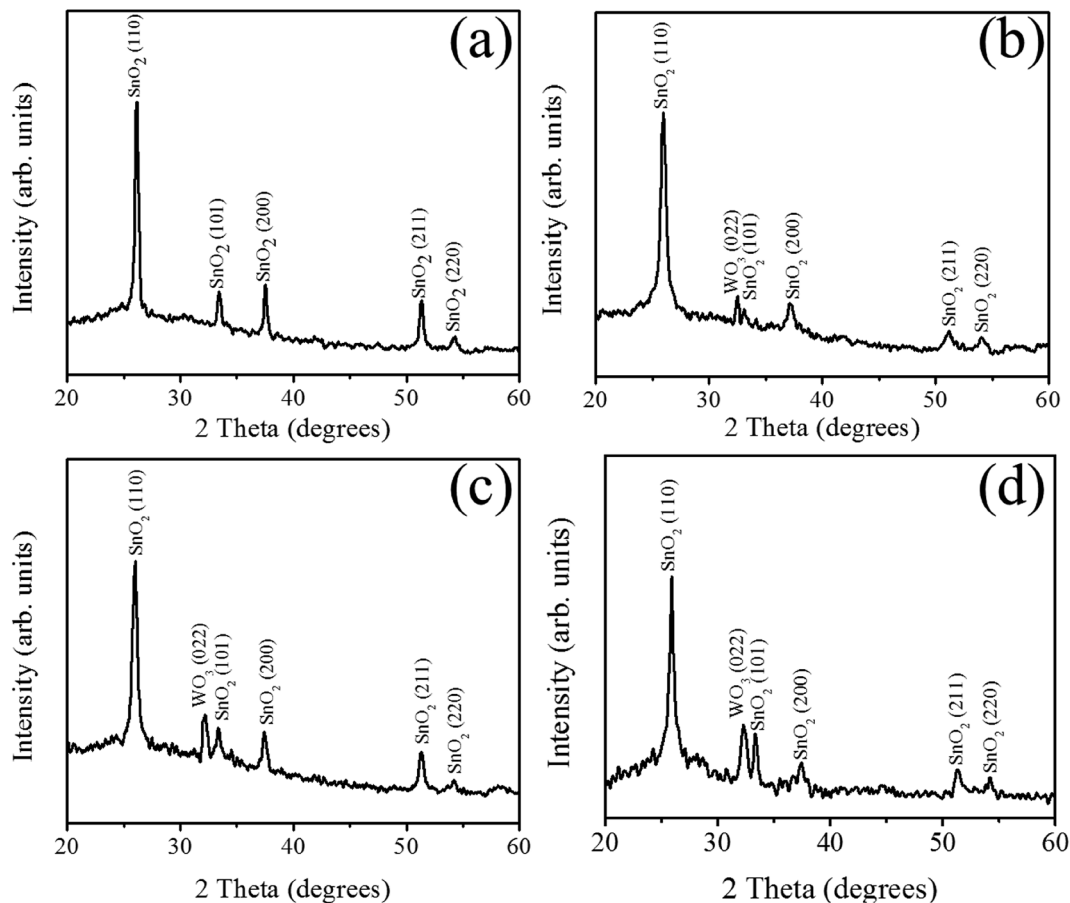
Fig. 1 (a) XRD pattern of the SnO_2 film and XRD patterns of SnO_2–WO_3 composite films prepared at various WO_3 sputtering powers: (b) 35 W, (c) 50 W, (d) 65 W.

growth of the composite films with an increased sputtering power of WO_3. The average SnO_2 crystallite size was decreased from 20 in the SnO_2 film to 8 nm in the composite film prepared at a WO_3 sputtering power of 65 W. Moreover, the WO_3 crystallites size in the composite films decreased from 15 to 11 nm when the sputtering power of WO_3 was increased from 35 W to 65 W, respectively. The decreased crystallite size of SnO_2 and WO_3 in the composite films might be associated with the restricted crystal growth of each SnO_2 and WO_3 crystallites during *in situ* cosputtering growth of the two-phase structure in the composite film.

Fig. 2(a)–(d) show SEM micrographs of the surface morphologies of the SnO_2 film and SnO_2–WO_3 composite films grown under various WO_3 sputtering powers. In Fig. 2(a)–(d), all the films display a homogenous crack-free appearance. From Fig. 2(a), the surface micrograph of the SnO_2 thin film shows the film composed of tiny, irregular crystallites; the film surface had a uniform and dense crystalline form. The surface morphology of the SnO_2–WO_3 composite film grown under a WO_3 sputtering power of 35 W is similar to that of the SnO_2 film (Fig. 2(b)); this might be associated with the trace content of WO_3 phase in the SnO_2–WO_3 composite film. Notably, the surface crystallites of the composite films prepared at the higher sputtering powers of

WO_3 (50 and 65 W) are the clusters composed of crystallites with different sizes. This surface feature is similar to the reported surface structure of the MnO_2–WO_3 composite films.[21] The agglomeration of the nanograins forms large surface clusters and are tightly packed in the composite films with the higher WO_3 sputtering power. The surface cluster feature coarsened with an increasing content of WO_3 phase in the SnO_2–WO_3 composite films are clearly demonstrated in the SEM micrographs. The average surface cluster sizes of the SnO_2–WO_3 composite films prepared at 50 W and 65 W sputtering power of WO_3 are 49 and 58 nm, respectively.

TEM was also used in this study to investigate the microstructures of SnO_2–WO_3 composite films prepared at the lowest and highest WO_3 sputtering powers. Fig. 3(a) shows a low-magnification cross-section TEM image of an SnO_2–WO_3 composite film grown with a WO_3 sputtering power of 35 W, which was composed of distinct columnar grains with diameters of 23–31 nm; no pores were visible on the film surface. Fig. 3(b) displays the selected-area electron diffraction (SAED) pattern from the SnO_2–WO_3 composite film. The presence of concentric rings that could be indexed to the (110), (200), (211), and (220) planes of tetragonal SnO_2 and the (022) plane of monoclinic WO_3 revealed that the composite film was of
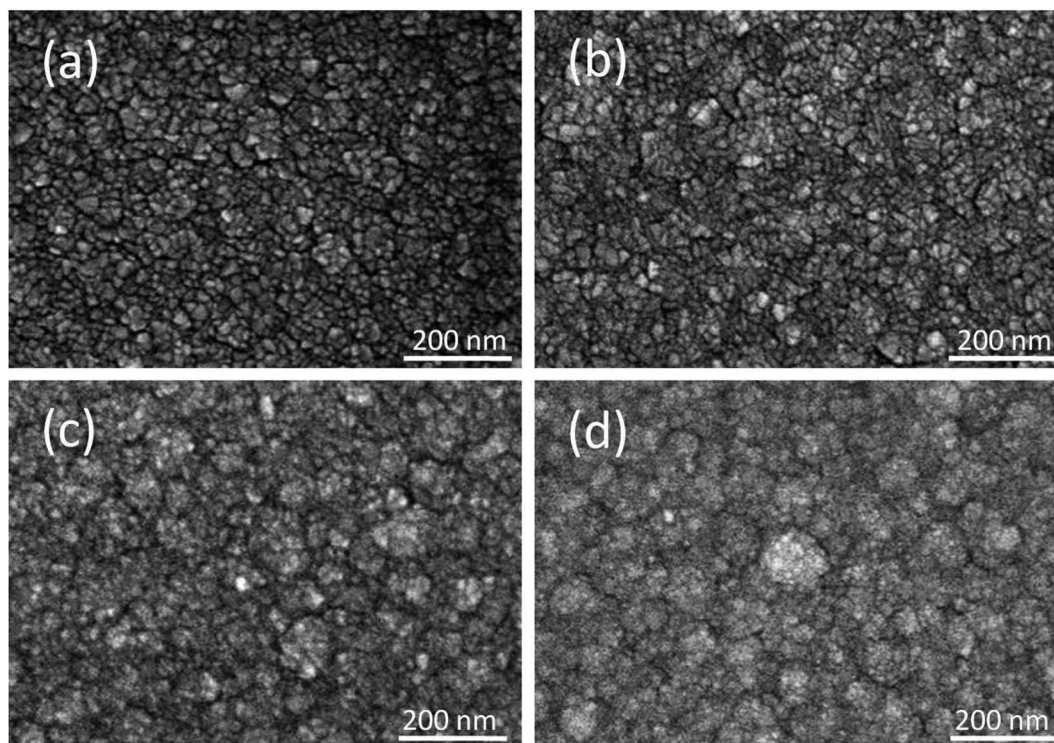
Fig. 2 (a) SEM image of the SnO_2 film. SEM images of SnO_2–WO_3 composite films prepared at various WO_3 sputtering powers: (b) 35 W, (c) 50 W, (d) 65 W.

a polycrystalline structure. A high-magnification image of a local region in the SnO_2–WO_3 composite film is shown in Fig. 3(c); the film had a thickness of approximately 100 nm, and grain boundaries between the columnar grains were visible. High-resolution (HR) TEM images from local regions of the composite film are also displayed in the insets of Fig. 3(c), with ordered and pronounced lattice fringes demonstrating that the composite film was highly crystalline. The long-range distributed lattice spacing of approximately 0.33 nm corresponded to the interplanar spacing of tetragonal SnO_2 (110). Moreover, some small regions with ordered lattice fringes had a lattice spacing of approximately 0.27 nm, which corresponded to the interplanar spacing of monoclinic WO_3 (022), revealing that SnO_2 constituted the major phase in the composite film. Fig. 3(d) shows energy-dispersive X-ray spectroscopy (EDS) spectra obtained from the SnO_2–WO_3 composite film, verifying that Sn, W, and O were the major elemental components of the sample. The W content in the composite film was estimated at approximately 5.1 at%.

Fig. 4(a) shows a low-magnification cross-section TEM image of the SnO_2–WO_3 composite film prepared with a WO_3 sputtering power of 65 W. The composite film was dense and homogeneously thick throughout the cross-section; the film thickness was approximately 95 nm. Fig. 4(b) shows this composite film's SAED pattern, to which various crystallographic planes of tetragonal SnO_2 and monoclinic WO_3 (022) were indexed; these crystallographic planes were consistent with the XRD result. The high-magnification TEM image in

Fig. 4(c) reveals that the boundary between adjacent columnar grains was less pronounced than that observed in the composite film prepared at a WO_3 sputtering power of 35 W, indicating that the major SnO_2 crystalline film structure might slightly deteriorate with increasing WO_3 phase content in the composite film. HR images from local regions of the composite film exhibit the ordered lattice fringes of tetragonal SnO_2 (110) and monoclinic WO_3 (022). The EDS spectra in Fig. 4(d) show that the W content of the SnO_2–WO_3 composite film increased to approximately 12.1 at% at a WO_3 sputtering power of 65 W. The W content of composite films prepared at various WO_3 sputtering powers was also evaluated using XPS spectra, as illustrated in Table S1 and Fig. S1,† revealing that the composite films' W content evaluated using TEM-EDS was similar to that determined using XPS results.

Fig. 5(a)–(e) illustrates changes in the water contact angle on the surface of SnO_2, WO_3, and composite SnO_2–WO_3 films with varying WO_3 content. Fig. 5(a) shows that the contact angle of the SnO_2 thin film was measured at approximately 87°, whereas Fig. 5(b) demonstrates that the WO_3 thin film exhibited a contact angle of approximately 69°. The morphology of the solid films could affect their measured contact angle. In this study, the WO_3 film was more hydrophilic than the SnO_2 film. Incorporation of the WO_3 phase into the SnO_2 matrix should cause SnO_2–WO_3 composite films to exhibit a smaller contact angle than that of the pure SnO_2 film,[22] as shown in Fig. 5(c)–(e). Moreover, the contact angle of the composite film decreased from 61° to 46° as the WO_3 sputtering power increased from 35
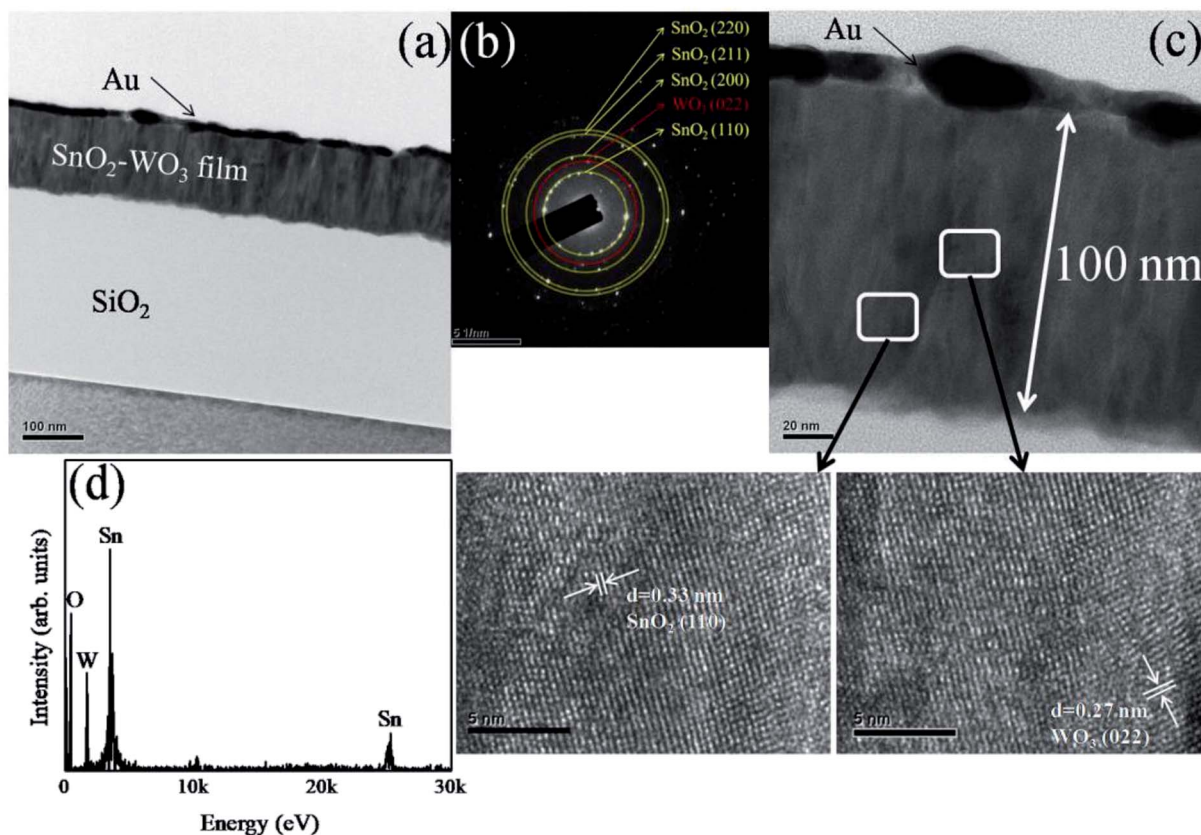
Fig. 3 TEM analyses of the SnO_2–WO_3 composite film prepared at the WO_3 sputtering power of 35 W: (a) low-magnification TEM image. (b) SAED pattern. (c) High-magnification image. The HRTEM images taken from the local regions of the film are shown in the insets. (d) EDS spectra of Sn, W, and O elements taken from the film.

to 65 W, respectively. Fig. 5(d) and (e) shows that the contact angles were substantially smaller than that of WO_3 film. A pronounced surface morphology difference between the WO_3 film and the SnO_2–WO_3 composite films with higher WO_3 content, prepared at WO_3 sputtering powers of 50 and 65 W, might account for this result. A nanograin agglomeration forming large surface clusters was observed on the SnO_2–WO_3 composite films with high WO_3 sputtering powers (50 and 65 W), which differed considerably from the surface of the WO_3 film. The numerous nanograins on the surface clusters of the composite films enhanced their ability to retain absorbed water, resulting in increased hydroxyl content of these films. The nanocomposite films prepared at WO_3 sputtering powers of 50 and 65 W thus exhibited increased hydrophilicity compared with the pure WO_3 film. A similar surface feature-dependent change in hydrophilicity was reported in Ti anodic oxidation formation of TiO_2, consistent with the prediction of the Wenzel theoretical model.[23]

Fig. 6(a) presents a comparison of optical absorbance curves for the SnO_2, WO_3, and composite SnO_2–WO_3 films. Because of the wide bandgap energies of SnO_2 and WO_3 in the UV region, the optical absorbance edges of these films were located in that region. The bandgap values of the synthesized SnO_2 and WO_3 thin films were evaluated using the Tauc plots in Fig. 6(b) and (c),[24] respectively. The SnO_2 thin film's bandgap was

approximately 3.61 eV, whereas that of the WO_3 thin film had a relatively small bandgap of 3.49 eV. Coupling of the SnO_2 matrix with the WO_3 phase in the composite film might account for the narrower optical bandgap of the composite films, as shown in Fig. 6(a). As the WO_3 phase content in the composite thin films increased, a larger degree of redshift in their optical absorbance edge was observed, indicating that the light-harvesting ability of the SnO_2 thin film was enhanced by incorporating the WO_3 phase.

Absorbance spectra of the RhB solution after 30, 60, 90, and 120 min of irradiation in the presence of SnO_2, WO_3, and different composite SnO_2–WO_3 films are shown in Fig. 7(a)–(d). RhB has a characteristic absorption band at approximately 551 nm. The absorbance spectra intensity of the RhB solution containing various thin-film samples decreased with an increased duration of irradiation. The degradation percentage of RhB absorbance spectra intensity *versus* the irradiation duration for the RhB solution containing various thin-film samples is shown in Fig. 7(e). Notably, after 120 min, degradation reached approximately 75–90% for the SnO_2–WO_3 composite films, highlighting their superior photodegradation ability compared with the SnO_2 and WO_3 films. Moreover, as the WO_3 content in SnO_2–WO_3 composite films increased, the degradation rate significantly improved. The separation efficiency of photoexcited carriers in the SnO_2, WO_3, and composite
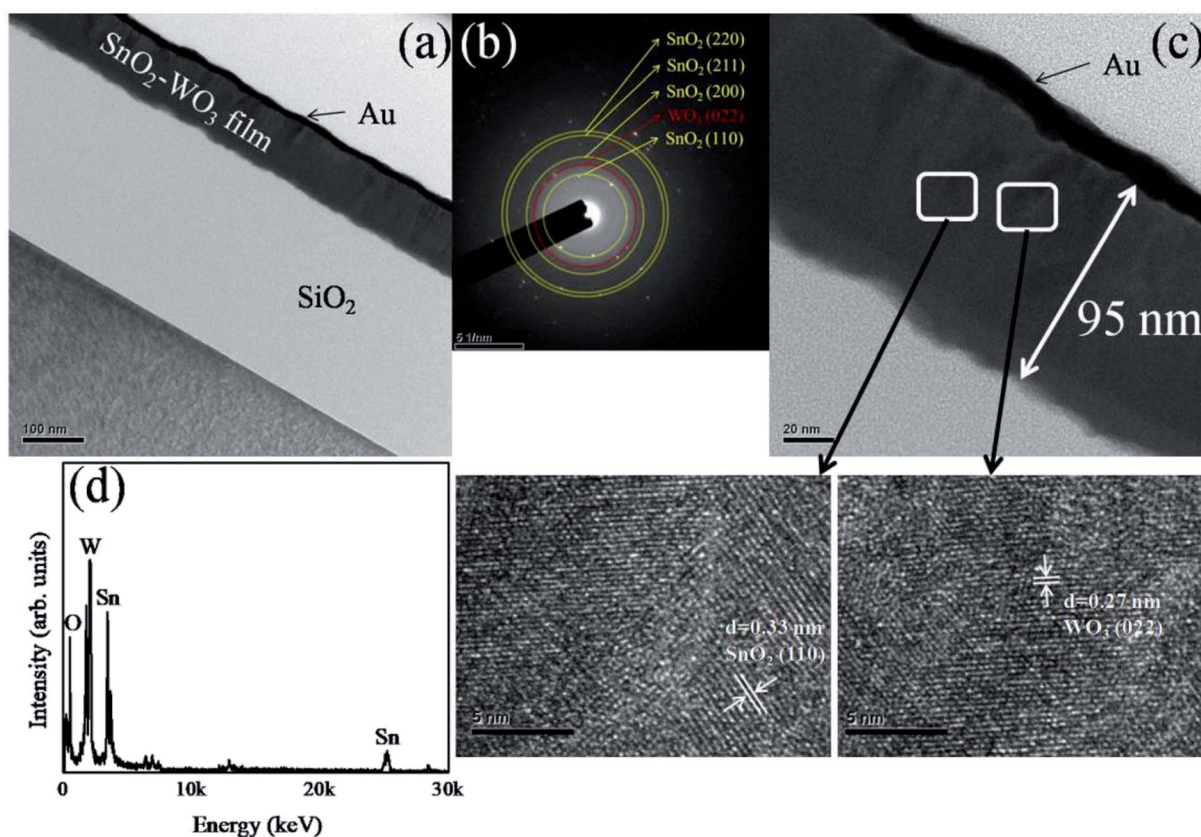
Fig. 4   TEM analyses of the SnO$_2$–WO$_3$ composite film prepared at the WO$_3$ sputtering power of 65 W: (a) low-magnification TEM image. (b) SAED pattern. (c) High-magnification image. The HRTEM images taken from the local regions of the film are shown in the insets. (d) EDS spectra of Sn, W, and O elements taken from the film.

SnO$_2$–WO$_3$ films was a key factor affecting the photo-degradation rate of these thin-film photocatalysts. Formation of a type II band alignment between the SnO$_2$ and WO$_3$ contact regions in the composite films enhanced photoexcited carrier separation efficiency relative to the composite film constituents (SnO$_2$ and WO$_3$). This could explain the superior RhB dye photodegradation ability of composite films. A possible mechanism for the improved photodegradation ability of composite
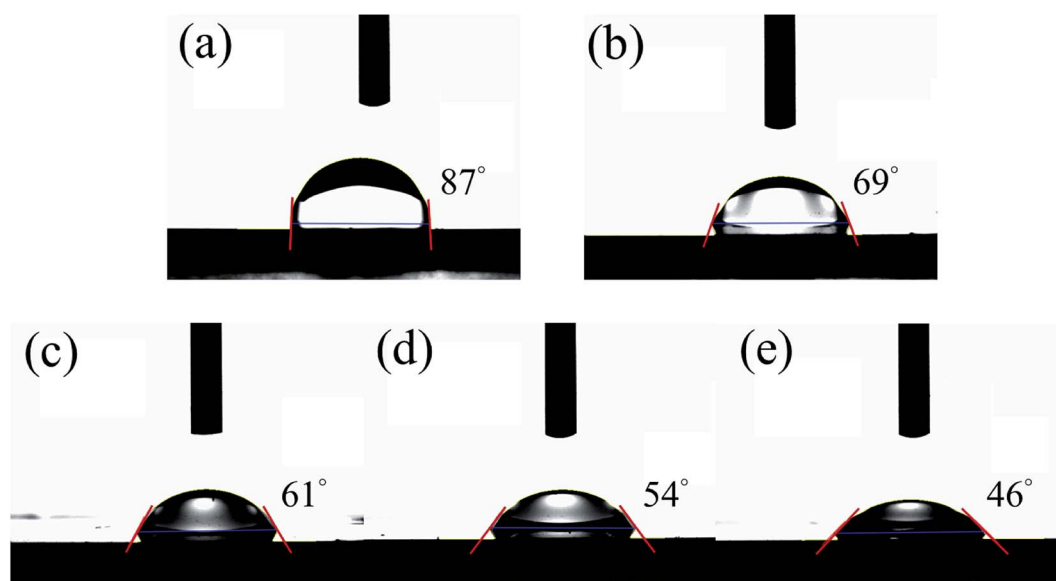

Fig. 5   (a) and (b) are water contact angle results on the SnO$_2$ and WO$_3$ films, respectively. (c), (d), and (e) are water contact angle results on the SnO$_2$–WO$_3$ composite films prepared at the WO$_3$ sputtering powers of 35, 50, and 65 W, respectively.
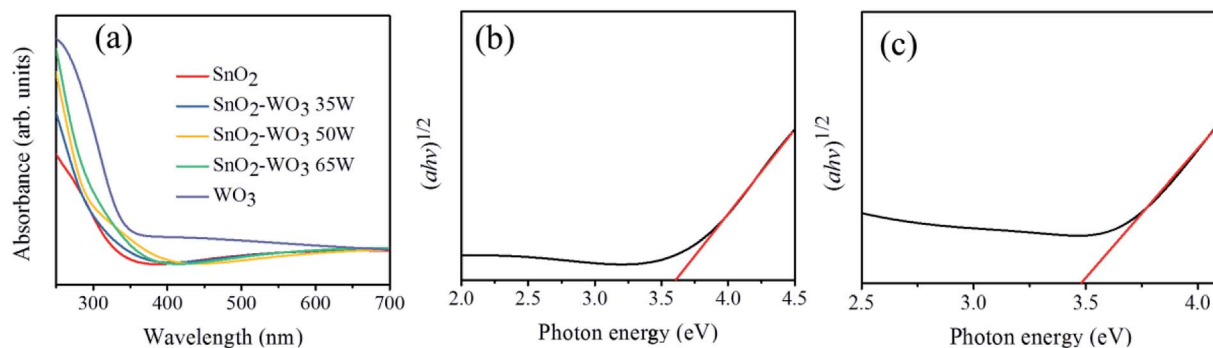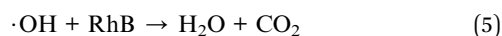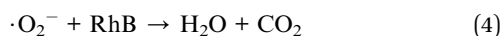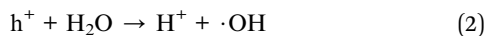
Fig. 6 (a) UV-Vis absorbance spectra of the SnO_2, WO_3, and various SnO_2–WO_3 films. (b) Tauc plot of the SnO_2 film. (c) Tauc plot of the WO_3 film.

films is illustrated in Fig. 8(f). Electrons and holes were generated in both the SnO_2 and WO_3 phases of composite films under irradiation. According to the bandgap energies, the conduction band (CB) edge potential of WO_3 is more negative than that of SnO_2.[15] Therefore, photogenerated electrons in WO_3 would easily transfer to SnO_2 before recombination, whereas the holes would move in the opposite direction, namely, from the valence band of SnO_2 to WO_3, resulting in effective charge separation. The greater number of free carriers in the composites than in individual SnO_2 and WO_3 thin films increased the degree of surface reaction to RhB dyes in the thin-film samples under irradiation. Oxygen, which can accept electrons and combine with hydrogen, produced H_2O on the film surface. The electrons accumulating in the CB of SnO_2 could be transferred to the adsorbed oxygen, thus yielding $\cdot O_2^-$, which then further reacted to finally produce the active $\cdot OH$ radical; moreover, the holes transferred to WO_3 oxidized H_2O molecules to yield hydroxyl radicals, according to the following reactions:

$$e^- + O_2 \rightarrow \cdot O_2^- \tag{1}$$

$$h^+ + H_2O \rightarrow H^+ + \cdot OH \tag{2}$$

$$OH^- + h^+ \rightarrow \cdot OH \tag{3}$$

$$\cdot O_2^- + RhB \rightarrow H_2O + CO_2 \tag{4}$$

$$\cdot OH + RhB \rightarrow H_2O + CO_2 \tag{5}$$

Consequently, $\cdot O_2^-$ and $\cdot OH$ acted as effective oxidants and reacted with RhB on the surface of the SnO_2–WO_3 composite films. Similar band alignment effects of decreasing the recombination rate of photogenerated carriers have been demonstrated in SnO_2–ZnO heterostructured fibers and TiO_2–WO_3 nanostructures, which improve photodegradation ability toward organic dyes.[25,26] The SnO_2–WO_3 composite film prepared at a WO_3 sputtering power of 65 W exhibited the highest degradation ability among the composite film samples, which was attributable to several factors. First, composite film prepared at a WO_3 sputtering power of 65 W exhibited a superior hydrophilicity to those prepared at other WO_3 sputtering powers. It has been shown that the higher photocatalytic activity

exhibited in a TiO_2–SnO_2 composite film, compared with a pure TiO_2 film, was attributable to enhanced hydrophilicity in the composite film.[11] Second, a larger degree of redshift of the SnO_2 matrix adsorption edge with increased WO_3 content was observed. A higher degree of light harvesting and thin film surface hydrophilicity accounted for the superior photodegradation ability of the composite film prepared at a WO_3 sputtering power of 65 W. The photodegradation stability of this composite film under irradiation in the RhB solution was evaluated after its recycling (Fig. 7(g)), and after five test cycles it was found to have maintained relatively consistent activity, without apparent deactivation.

Fig. 8 illustrates the temperature-dependent ethanol gas-sensing response curves of the SnO_2, WO_3, and composite SnO_2–WO_3 films on exposure to 100 ppm ethanol. The optimal operating temperature of the semiconductors is associated with a resultant equilibrium between surface reaction with ethanol vapor and the diffusion of ethanol vapor to the surface of the materials.[1] An optimal operating temperature of the SnO_2 thin film was 325 °C in this study. Furthermore, the highest ethanol gas-sensing response for the WO_3 thin film was reached at the operating temperature of 350 °C which is the maximum temperature of the measurement system. The high operating temperature of 350 °C for the WO_3 thin film to detect ethanol vapor with a visible response is similar to the previous work.[27] Comparatively, the SnO_2 thin film is more sensitive to detect ethanol vapor at the relatively lower operating temperature. The higher WO_3 phase content in the composite film prepared at the WO_3 sputtering power of 65 W deteriorated the performance of the optimal operating temperature and gas-sensing response compared with the SnO_2 thin-film matrix. By contrast, the composite films prepared at the WO_3 sputtering powers below 50 W exhibited the lower optimal operating temperature at 300 °C. The decreased optimal operating temperature of the composite films prepared at the WO_3 sputtering power below 50 W might be associated with the proper potential barrier numbers in the composite films that decreased the optimal operating temperature and also increased the gas-sensing responses in comparison with those of the SnO_2 thin film.

Fig. 9(a)–(e) shows the typical dynamic gas response curves of the SnO_2, WO_3, and composite SnO_2–WO_3 films for various
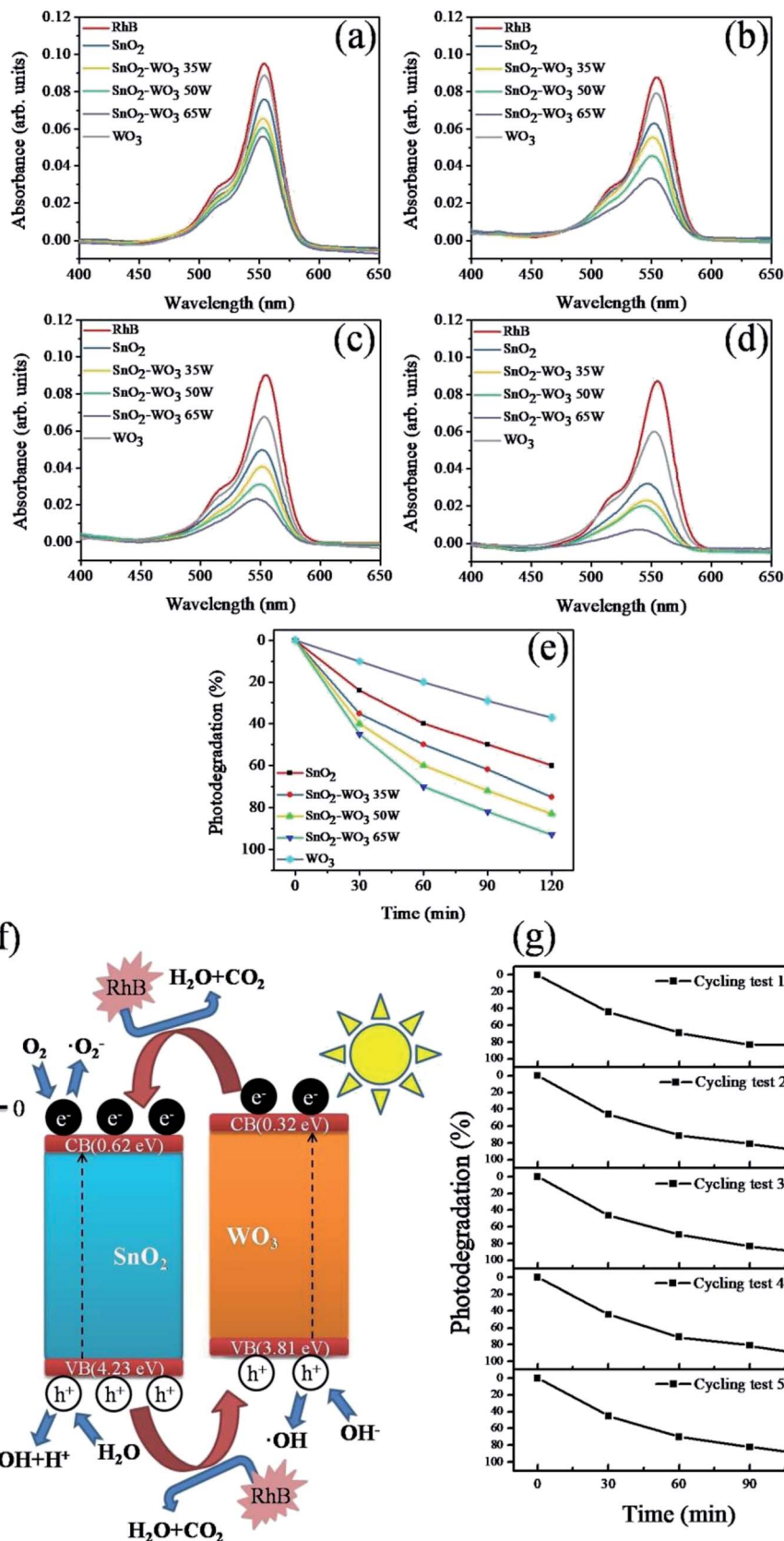
Fig. 7 The absorbance spectra of the RhB solution containing various thin-film samples under different irradiation durations: (a) 30 min. (b) 60 min. (c) 90 min. (d) 120 min. (e) Percentage photodegradation *vs.* irradiation duration of the RhB solution containing various thin-film samples. (f) Illustration of photodegradation mechanism for the SnO_2–WO_3 composite film to RhB dyes. (g) Recycled performances in the presence of the SnO_2–WO_3 film prepared at 65 W sputtering power of WO_3 for photodegrading RhB dyes.
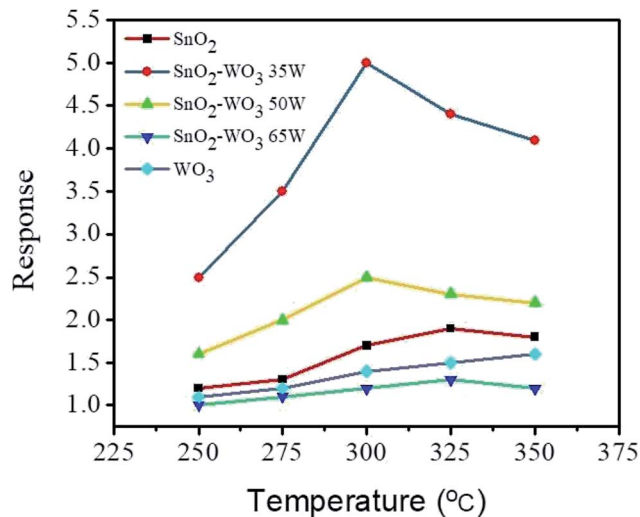
Fig. 8 Temperature-dependent 100 ppm ethanol gas-sensing responses of the SnO$_2$–WO$_3$ composite film prepared at 35 W sputtering power of WO$_3$.

concentrations of ethanol vapor (100 to 1000 ppm). The n-type conduction of these oxide films induces oxygen molecules adsorbed on their surface to extract electrons from their CB and became adsorbed oxygen ions on that surface. An electron depletion layer should be formed in the surface region of these films, which increases their electrical resistance. The reaction of ethanol vapor with the adsorbed oxygen ions on n-type oxide films is well documented.[1] When reducing gas molecules such as ethanol vapor are introduced on the film surface, the adsorbed oxygen ions release electrons to the film, further reducing its electrical resistance. Fig. 9(a)–(e) shows that the SnO$_2$, WO$_3$, and composite SnO$_2$–WO$_3$ films exhibited a concentration-dependent ethanol gas-sensing response; namely, higher ethanol vapor concentrations resulted in a higher gas-sensing response. This is attributable to the fact that more ethanol molecules react with more adsorbed oxygen ions on the film surface, thus producing a higher gas-sensing response. Moreover, the SnO$_2$, WO$_3$, and composite SnO$_2$–WO$_3$ films demonstrated various degrees of gas-sensing ability to the ethanol vapor, as shown in Fig. 9(a)–(e). The ethanol gas-sensing responses of these films on exposure to various ethanol vapor concentrations are summarized in Fig. 9(f). Notably, the gas-sensing response of the SnO$_2$ film on exposure to 100–1000 ppm ethanol vapor ranged from 1.8 to 2.5, relative to which the WO$_3$ film demonstrated a poorer ethanol gas-sensing ability, with responses ranging from 1.4 to 2.0 when exposed to 100–1000 ppm ethanol vapor. The SnO$_2$–WO$_3$ composite films prepared at a WO$_3$ sputtering power of 35 and 50 W demonstrated enhanced gas-sensing ability compared with their constituent SnO$_2$ and WO$_3$ films. Moreover, the highest ethanol gas-sensing response was observed for the SnO$_2$–WO$_3$ composite film prepared at a WO$_3$ sputtering power of 35 W, attaining gas-sensing responses of 5.1 and 8.3 on exposure to 100 and 1000 ppm of ethanol vapor, respectively. However, as shown in Fig. 9(f), ethanol gas-sensing response rapidly

declined when the SnO$_2$–WO$_3$ composite film was prepared at the highest sputtering power of 65 W. This composite film's gas-sensing response was even poorer than that of the individual SnO$_2$ and WO$_3$ films. Comparison of gas-sensing performance demonstrated that a slight increase in WO$_3$ content (preparation at a WO$_3$ sputtering power of 35 W) led to a marked improvement in the SnO$_2$–WO$_3$ composite film's gas-sensing response. Partial addition of a WO$_3$ phase into the SnO$_2$ matrix caused formation of heterojunctions between SnO$_2$ and WO$_3$ crystals. These SnO$_2$–WO$_3$ heterojunctions in turn caused depletion regions to form at heterointerfaces, thereby increasing the number of potential barriers in the composite film. An optimal loading content of ZnO particles in SnO$_2$ tubes was reported to improve gas-sensing responses. This phenomenon is closely associated with modulation of the local depletion layer in SnO$_2$/ZnO contact regions on exposure to target gases.[28] Notably, the ethanol gas-sensing response of the SnO$_2$–WO$_3$ composite film prepared at 35 W sputtering power of WO$_3$ on exposure to 20 ppm ethanol (the minimum ethanol concentration in the measurement system) was still visible and the response reached 2.1. Additionally, response and recovery times of the SnO$_2$–WO$_3$ composite films were defined as the durations required for occurrence of a 90% change in resistance on exposure to ethanol gas (response) and air (recovery), respectively. Response times for the SnO$_2$–WO$_3$ composite film prepared at a WO$_3$ sputtering power of 35 W when exposed to various ethanol vapor concentrations (100–1000 ppm) ranged from 6 to 11 s, whereas recovery times ranged from 61 to 71 s. Response times for the composite film prepared at 50 W ranged from 14 to 20 s, whereas those for the composite film prepared at 65 W ranged from 16 to 40 s. Recovery times for the composite films prepared at WO$_3$ sputtering powers of 50 and 65 W all exceeded 80 s. Notably, response times for the SnO$_2$ film were in the range of 11–14 s, and recovery times in the range of 72–153 s. The improved sensing speed of the SnO–WO$_3$ composite film prepared at a WO$_3$ sputtering power of 35 W was thus evident. Fig. 9(g) shows cyclic gas-sensing test results for the composite film prepared at a WO$_3$ sputtering power of 35 W when exposed to 750 ppm of ethanol vapor. Stable sensing behavior over five test cycles was observed for this composite film, demonstrating its high stability and reproducibility for ethanol vapor detection. The gas-sensing selectivity of the film was further investigated on exposure to various oxidizing and reducing target gases in Fig. 9(h). The result demonstrated that the SnO$_2$–WO$_3$ composite thin film was more sensitive to detect ethanol vapor in this study. Table 1 summarizes the ethanol gas-sensing performances of the reported SnO$_2$–WO$_3$ composite film and other SnO$_2$-based composite films prepared using various methods upon exposure to various ethanol vapor concentrations at the sensor operating temperatures of 300 °C.[29–31] Comparatively, ethanol gas-sensing responses of the SnO$_2$–WO$_3$ composite film prepared at a WO$_3$ sputtering power of 35 W in this work exhibited a superior gas-sensing response than did those under similar gas-sensing test conditions in previous studies.

The ethanol gas-sensing mechanisms of pure SnO$_2$ and SnO$_2$–WO$_3$ composites with adequate WO$_3$ phase content in this study
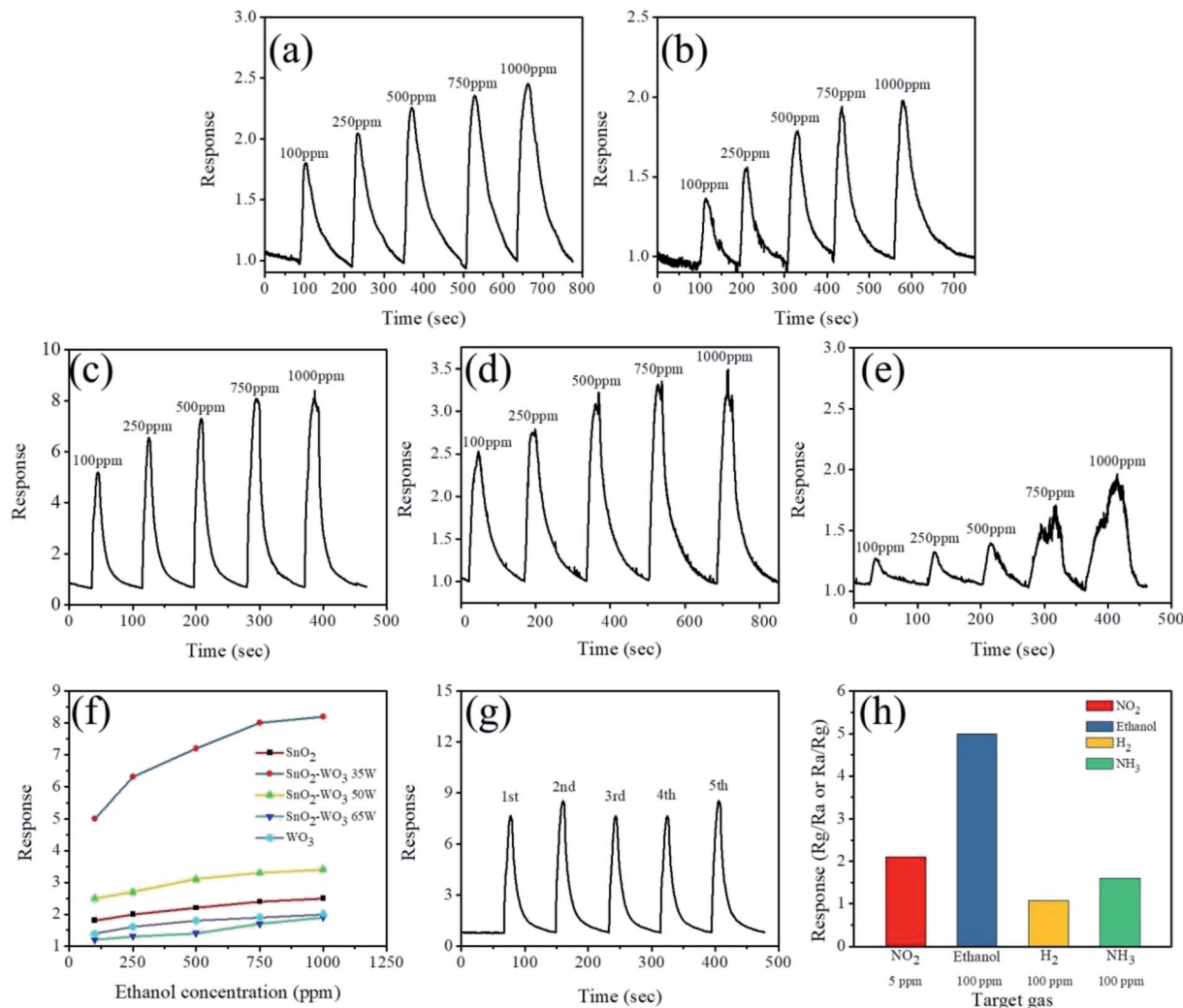
Fig. 9 (a) and (b) are ethanol gas-sensing response curves of the SnO_2 and WO_3 films, respectively. (c), (d), and (e) are gas-sensing response curves of the SnO_2–WO_3 films prepared at WO_3 sputtering powers of 35, 50, and 65 W, respectively. (f) Gas-sensing response values *vs.* ethanol vapor concentrations for various thin films. (g) Cyclic gas-sensing response curves for the SnO_2–WO_3 film prepared at 35 W sputtering power of WO_3 on exposure to 750 ppm ethanol vapor. (h) Gas sensing selectivity histogram of the SnO_2–WO_3 composite film prepared at 35 W sputtering power of WO_3 on exposure to 5 ppm NO_2 and 100 ppm of H_2 and NH_3.

are shown in Fig. 10. Surface depletion regions in SnO_2 and WO_3 crystals and SnO_2/WO_3 crystal contact regions formed various potential barrier heights. In a gas-sensing test, higher numbers of surface potential barriers may be expected to act with ethanol vapor molecules in the composite film than in the pure SnO_2 film.

Therefore, a higher degree of resistance variation is observed on exposure to ethanol vapor in the SnO_2–WO_3 composite film with adequate WO_3 phase content. Higher ethanol gas-sensing responses were observed for this composite film than for the pure SnO_2 film in given gas-sensing test conditions.

Table 1 Ethanol gas-sensing performance of various SnO_2–WO_3 and other SnO_2-based composite films prepared using various methods upon exposure to ethanol vapor at the optimal temperature of 300 °C (ref. 29–31)

Composite film	Synthesis method	Optimal temperature (°C)	Concentration (ppm)	Response (R_a/R_g)	Detection limit (ppm)	Response/recovery time (sec)
SnO_2–WO_3	Hydrothermal method	300	200	1.39	N/A	180/200
SnO_2–ZnO	Hydrothermal method	300	200	4.5	20	72/900
SnO_2–WO_3 (this work)	**Cosputtering**	**300**	**250**	**6.5**	**20**	**7/63**
SnO_2–CeO_2	Sol–gel method	300	800	7.8	30	60/600
SnO_2–WO_3 (this work)	**Cosputtering**	**300**	**750**	**8**	**20**	**9/67**
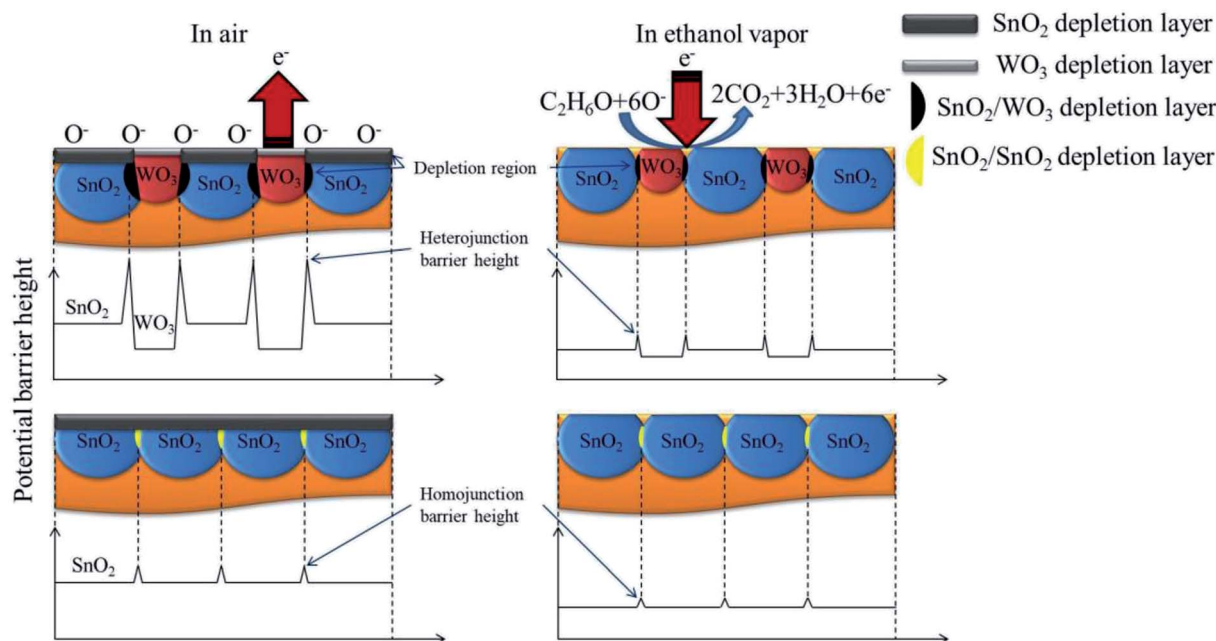
Fig. 10 Schematics of ethanol gas-sensing mechanisms for the SnO_2 and SnO_2–WO_3 films.

Conclusions

In this study, SnO_2–WO_3 nanocomposite films with various WO_3 phase contents were prepared by rf cosputtering metallic Sn and ceramic WO_3 targets. The W content of the resulting SnO_2–WO_3 composite films was varied from 5.4 at% to 12.3 at% through different WO_3 sputtering powers. Structural analysis indicated that high WO_3 phase content degraded the SnO_2 matrix's crystalline quality in the composite films, with surface crystallites in these films becoming coarser. Moreover, a higher light harvesting ability of the composite films was observed with higher WO_3 phase content. The SnO_2–WO_3 composite films exhibited superior RhB dye photodegradation ability relative to their constituents. Ethanol gas-sensing tests revealed that the addition of suitable WO_3 crystals (W content of 5.4 at%) to the SnO_2 matrix improved the gas-sensing response. The heterogeneous potential barriers in the composite films play an essential role in their ethanol gas-sensing behavior.

Conflicts of interest

There are no conflicts to declare.

Acknowledgements

References

1 Y. C. Liang, C. M. Lee and Y. J. Lo, *RSC Adv.*, 2017, **7**, 4724–4734.
2 D. Hanft, M. Bektas and R. Moos, *Materials*, 2018, **11**, 1342.
3 A. Bhattacharjee and Md. Ahmaruzzaman, *RSC Adv.*, 2015, **5**, 66122–66133.
4 A. Zarkov, A. Stanulis, L. Mikoliunaite, A. Salak and A. Kareiva, *Thin Solid Films*, 2018, **649**, 219–224.
5 S. Ben Ameur, H. Belhadjltaief, A. Barhoumi, B. Duponchel, G. Leroy, M. Amlouk and H. Guermazi, *Vacuum*, 2018, **155**, 546–552.
6 Talinungsang, D. D. Purkayastha and M. G. Krishna, *Appl. Surf. Sci.*, 2018, **447**, 724–731.
7 P. S. Kolhe, P. M. Koinkar, N. Maiti and K. M. Sonawane, *Phys. B*, 2017, **524**, 90–96.
8 Y. C. Liang and Y. J. Lo, *RSC Adv.*, 2017, **7**, 29428–29439.
9 K. Suematsu, N. Ma, M. Yuasa, T. Kida and K. Shimanoe, *RSC Adv.*, 2015, **5**, 86347–86354.
10 H. S. Jeong, M. J. Park, S. Kwon, H. J. Joo, S. H. Song and H. I. Kwon, *Ceram. Int.*, 2018, **44**, 17283–17289.
11 Q. Liu, X. Wu and B. Wang, *Mater. Res. Bull.*, 2002, **37**, 2255–2262.
12 G. Xie, J. Yu, X. Chen and Y. Jiang, *Sens. Actuators, B*, 2007, **123**, 909–914.
13 P. Dong, B. Yang, C. Liu, F. Xu, X. Xi, G. Hou and R. Shao, *RSC Adv.*, 2017, **7**, 947–956.
14 D. Valerini, S. Hernández, F. Di Benedetto, N. Russo, G. Saracco and A. Rizzo, *Mater. Sci. Semicond. Process.*, 2016, **42**, 150–154.
15 J. H. Baek, B. J. Kim, G. S. Han, S. W. Hwang, D. R. Kim, I. S. Cho and H. S. Jung, *ACS Appl. Mater. Interfaces*, 2017, **9**, 1479–1487.
16 A. K. Nayak, R. Ghosh, S. Santra, P. K. Guha and D. Pradhan, *Nanoscale*, 2015, **7**, 12460–12473.
17 M. Yin, M. Yao, H. Fan and S. Liu, *J. Alloys Compd.*, 2018, **736**, 322–331.

18 H. Abdul-Ameer, M. AL-Hilli and M. Khalaf, *Baghdad Sci. J.*, 2018, **15**, 227–233.

19 A. A. Najim, S. S. Shaker and M. A. H. Muhi, *Plasmonics*, 2017, **12**, 1051–1055.

20 V. Madhavi, P. Kondaiah, O. M. Hussain and S. Uthanna, *Phys. B*, 2014, **454**, 141–147.

21 C. Zhang, A. Boudiba, C. Navio, M.-G. Olivier, R. Snyders and M. Debliquy, *Sens. Actuators, B*, 2012, **161**, 914–922.

22 N. Naseri, R. Azimirad, O. Akhavan and A. Z. Moshfegh, *J. Phys. D: Appl. Phys.*, 2007, **40**, 2089–2095.

23 B. Li, J. Li, C. Liang, H. Li, L. Guo, S. Liu and H. Wang, *Rare Met. Mater. Eng.*, 2016, **45**, 858–862.

24 Y. C. Liang and C. M. Lee, *J. Appl. Phys.*, 2016, **120**, 135306.

25 X. Chen, F. Zhang, Q. Wang, X. Han, X. Li, J. Liu, H. Lin and F. Qu, *Dalton Trans.*, 2015, **44**, 3034–3042.

26 B. Lu, X. Li, T. Wang, E. Xie and Z. Xu, *J. Mater. Chem. A*, 2013, **1**, 3900–3906.

27 S. Roy, A. Dey, B. Biswas and S. K. Sarkar, *J. Mater. Eng. Perform.*, 2018, **27**, 2635–2642.

28 K. Diao, Y. Huang, M. Zhou, J. Zhang, Y. Tang, S. Wang, T. Liu and X. Cui, *RSC Adv.*, 2016, **6**, 28419–28427.

29 S. J. Kim, P. Cho, J. H. Lee, C. Y. Kang, J. S. Kim and S. J. Yoon, *Ceram. Int.*, 2008, **34**, 827–831.

30 K. W. Kim, P. S. Cho, S. J. Kim, J. H. Lee, C. Y. Kang, J. S. Kim and S. J. Yoon, *Sens. Actuators, B*, 2007, **123**, 318–324.

31 F. Pourfayaz, A. Khodadadi, Y. Mortazavi and S. Mohajerzadeh, *Sens. Actuators, B*, 2005, **108**, 172–176.